Design of High Power Density and High Efficiency Wound-Field Synchronous Motor for Electric Vehicle Traction

HYEON-JIN PARK[1] AND MYUNG-SEOP LIM[2]
[1]Department of Automotive Engineering, Hanyang University, Seoul 04763, South Korea
[2]School of Mechanical Engineering, Yeungnam University, Gyeongbuk 38541, South Korea

Corresponding author: Myung-Seop Lim (limmang87@yu.ac.kr)

ABSTRACT This paper deals with a design method to improve the power density and energy efficiency of a wound-field synchronous motor (WFSM) using hairpin type rectangular wire for electric vehicle traction. First, the prototype is analyzed via experiments to come up with plans to improve it. In addition, mechanical loss of the prototype including the bearing and brush friction losses is obtained and used for designing the improved motor. After then, an analytical approach is presented for the magnetic circuit design to minimize magnetic resistance in the motor core. Also, the analytical methods are proposed to predict the resistance of the field and armature windings. At this step, rectangular wire is considered for the armature winding to reduce the copper loss. Moreover, the calculation process is presented to estimate the iron loss considering harmonics. The performances such as power density and efficiency of the improved WFSM are analyzed and compared with those of the prototype. In addition, the energy efficiency of the motors in the new European drive cycle (NEDC) is analyzed. Finally, the performances of the improved WFSM are compared with the experimental results to verify the validity of the proposed design process.

I. INTRODUCTION

Recently, on account of high efficiency and power density, interior permanent magnet synchronous motors (IPMSMs) using rare-earth magnets have been applied as traction motors for electric vehicles (EVs) [1]. However, the issues related to the rare-earth magnets, which is high cost and unstable supply, have brought the development of various motors without rare-earth materials such as neodymium and dysprosium. In particular, as IPMSMs are operated at high-speed, high-voltage terminals can be generated due to the shortage of control in power electronics and this leads supplementary protection systems to disconnect the motors from the network for the damage limit on the vehicles. This problem can be solved with a wound-field synchronous motor (WFSM) [2]–[4]. Nevertheless, the efficiency of a WFSM is lower than that of an IPMSM because of the losses incurred on the coil and brush of the rotor.

The associate editor coordinating the review of this manuscript and approving it for publication was Xiaodong Sun.
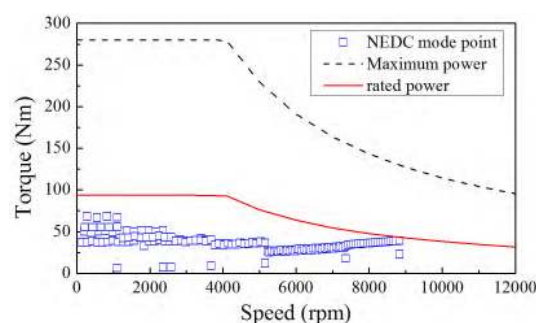

FIGURE 1. New European Drive Cycle (NEDC).

This study focuses on the design of a WFSM for enhancing the power density as well as energy efficiency in the new European drive cycle (NEDC) mode. The NEDC mode has been widely employed for testing and evaluating systems for EVs in Europe [5]–[10]. Fig. 1 displays the torque-speed relationship to which the NEDC mode has been applied. The details of the design process are explained as follows.

At first, the performance of the existing WFSM i.e., the prototype, is analyzed via the experiment to come up with plans to improve it. In addition, mechanical loss of the prototype including bearing friction loss and windage loss is measured through the no-load experiment. The mechanical loss calculated from the no-load test result is considered to design the improved WFSM.

Secondly, the geometric design methods and material selection processes are presented in order to increase both the torque density and efficiency of the WFSM [10]–[16]. If the stator core has high magnetic flux density, considerable iron loss is produced to meet the required performance of the WFSM. Moreover, the stator core with a high fill factor results in high winding resistance and, in turn, more copper loss. In order to solve these two problems, a method is suggested for determining the optimal turn number of the field and armature and the tooth and yoke widths. In addition, a hairpin winding is applied, and the electrical steel sheet considering magnetic saturation level is selected. As a result, such design methods can lower the winding resistance and magnetic flux density in the stator core. Especially, the fill factor increased by using the hairpin winding makes a significant contribution to the reduction of loss [17].

The third step is to accurately estimate design parameters such as flux linkage, inductance, and losses using finite elements analysis (FEA) and an analytical method [18]. The copper loss of both armature and field winding is calculated by Joule's First Law taking into account the operating temperature. The mechanical loss is determined via a no-load test of the prototype. The eddy current loss in its laminated iron core is considered in iron-loss data [19]. The iron loss, flux linkage, and inductance maps according to the load conditions are obtained using the armature and field currents. Map data is calculated for field currents of 0 to 15 A_{dc}, armature currents of 0 to 450 A_{rms}, and armature current phase angles of $-30°$ to $90°$.

Lastly, characteristics of the designed motor such as torque and power are analyzed by using the parameter analysis results in the third step. In addition, the efficiency map according to the load conditions as well as energy efficiency under the NEDC mode is calculated. As a result of the design method, both the NEDC efficiency and power density of the WFSM increased. The feasibility of the proposed design method and the design result is verified with the load and efficiency tests.

II. PROTOTYPE AND MECHANICAL LOSS
A. PROTOTYPE AND REQUIRED SPECIFICATIONS

The specifications for the prototype were obtained from the load test. The experimental setup for the test is shown in Fig. 2. The test was conducted by controlling the prototype's speed and load torque. The test results and the required specifications are given in Table 1. The power density was calculated considering not only the motor core but other components such as coil, bearing, brush, and slip ring, etc. Given
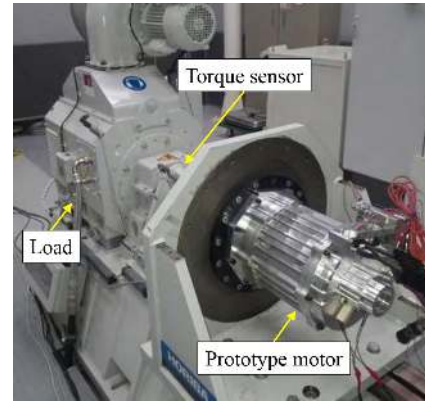

FIGURE 2. Test setup of the prototype.

TABLE 1. Specifications of the prototype.

Quantity	Unit	Prototype	Requirement
Power	kW	≥ 100	
Rated torque	Nm	280	
Max. speed	rpm	10,000	10,000
Field current	A_{dc}	13.5	14.5
Outer diameter	mm	215	21
Stack length	mm	128	≤ 120
Power density	kW/kg	2.12	≥ 2.2
Max. efficiency	%	96.5	≥ 96
Energy efficiency	%	93.7	≥ 94

these specifications, the efficiency of the machine is relevant, because there is considerable copper loss in the high-torque region, and iron loss increased significantly in the high-speed region. These losses are caused by the motor's magnetic saturation and winding resistance, and they are directly proportional to the current. Therefore, one of the critical design objectives is to determine the optimal features of the machine for reducing both iron and copper loss to maximize the efficiency as well as increasing power density.

B. MECHANICAL LOSS

The mechanical loss of the prototype including its bearing and brush friction losses were obtained via two different no-load tests. The reason for adopting these tests is that exact calculation of the mechanical loss is difficult and time-consuming as analytical methods and the FEA are applied. Especially, the mechanical loss data of the prototype obtained from the no-load tests can be used to design an improved machine. Firstly, no-load test was conducted with the prototype assembled with the brush and slip ring. The input power as the total no-load loss was calculated by multiplying the input current and the measured voltage of the machine. Secondly, only the dynamo system's friction loss was measured by using the same method. For this test to measure the dynamo friction torque only, however, the brush and slip ring were removed from the motor. Then, the mechanical loss was

calculated by subtracting the dynamo's friction loss from the total no-load loss [20]. During this process, copper loss was omitted because the square of the input current was negligibly small, and iron loss was also neglected because there was no magnetized iron core in the WFSM under the no-load condition. The calculated mechanical loss was ultimately used to design an improved model, as discussed in Section VI.

III. DETERMINATION OF THE CORE SHAPE
A. FIELD-TURN NUMBER
Magnetomotive force of the WFSM can be represented by the product of turn number and input current of the field winding. If the magnetomotive force is constant, the voltage can be derived in order to determine optimal turn number and input current. Moreover, as the magnetomotive force and current density are constant, slot area of the rotor can be determined in accordance with the turn number of the field winding. This value can be used as the criterion for determining the tooth and yoke widths of the rotor. Meanwhile, in case of the WFSM, the voltage induced by the field winding from the armature reaction at high speeds can interrupt direct-current control. Therefore, it is advantageous to lower the induced voltage when the motor is operated at high speed.

The equation for the field's induced voltage is as follows:

$$V_f = I_f R_f + \frac{d\lambda_f}{dt} \qquad (1)$$

Parameters can be used to build an equation in relation to the turn number in order to calculate the optimal value of the field's turn number. Assuming that the magnetomotive force and current density applied to the field are constant, the induced voltage equation can be expressed as follows:

$$V_f = N_f \left(\frac{l_{1-turn} J_f}{\sigma} + \frac{d\phi_f}{dt} \right) \qquad (2)$$

where,

$$F = N_f I_f = \text{constant} \qquad (3)$$

$$J_f = \frac{I_f}{A_{fieldcoil}} = \frac{F}{N_f A_{fieldcoil}} = \text{constant} \qquad (4)$$

$$R_f = \frac{l}{\sigma A_{fieldcoil}} \qquad (5)$$

$$l = N_f l_{1-turn} \qquad (6)$$

$$\frac{d\lambda_f}{dt} = N_f \frac{d\phi_f}{dt} \qquad (7)$$

In the preceding equation, V_f is the induced voltage of the field winding. N_f and I_f are the number of turns and current of the field winding, respectively. J_f is the current density of the field coil, and σ is the conductivity of the coil. F is the magneto-motive force. R_f is the resistance of the field winding. $A_{fieldcoil}$ and l_{1-turn} denote the cross-sectional area and the length of one turn of the field coil, respectively. l is total length of field coil considering the turn number. λ_f is the flux linkage of the field winding, and ϕ_f is the flux of the field winding.
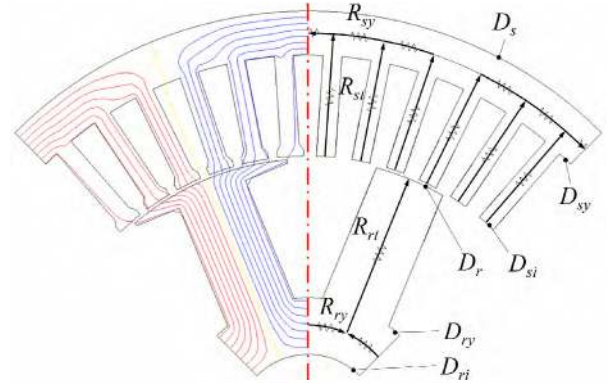

FIGURE 3. Magnetic circuit and equipotential line of the simplified WFSM model.

In other words, induced voltage can be reduced, and easier control is possible as less number of turns is applied. However, less number of turns requires a higher input current for the same magnetomotive force namely $N_f I_f$. Therefore, it is reasonable to determine magnetomotive force by minimizing the turn number within range of not exceeding the current limit. To achieve the same magnetomotive force 2092.5 A·turns of the prototype, thus, the turn number of the improved motor can be determined as 145 turns/pole because the input DC limit is 14.5 A. As a result, the slot area of the rotor became 590 mm². These results were reflected in the calculations of the rotor's tooth and yoke widths.

B. DETERMINATION OF THE TOOTH AND YOKE WIDTHS OF THE ROTOR AND STATOR CORES
The tooth and yoke widths of rotor and stator are obtained through an analytical method in this paper. Their values are used to minimize magnetic resistance in the magnetic circuit of the motor. Because the coils in the rotor are concentrated on one tooth, the flux through the tooth in the center is divided into two sides at the yoke, and the divided flux passes to the next tooth. However, as distributed winding is applied in the stator, the flux through several teeth is divided into two sides at the yoke, and the divided flux passes along the flux from the next several teeth to the teeth on the opposite pole side. The equipotential lines were shown in Fig. 3 to present these flux paths. In these cases, there are many fluxes with these paths flowing through the core of rotor and stator. The average flux path must be determined in order to obtain the average magnetic resistance. Therefore, assuming that the middle line of the path is the average flux path, it can be represented by the black arrows in Fig. 3. When this path is used as the magnetic circuit to derive the average magnetic resistance, (8)-(13) can be calculated:

$$R_{rm} = 2R_{rt} + R_{ry} \qquad (8)$$

$$R_{sm} = 2\frac{R_{st}^3 + 3R_{st}^2 R_{sy} + R_{st} R_{sy}^2}{3R_{st}^2 + 4R_{st} R_{sy} + R_{sy}^2} + R_{sy} \qquad (9)$$

where,

$$R_{rt} = \frac{2D_r - D_{ry} - D_{shaft}}{4\mu x_r L_{stk}}, \quad R_{ry} = \frac{\pi(D_{ry} + D_{ri}) - 2x_r s_{rn}}{\mu s_{rn} L_{stk}(D_{ry} - D_{ri})} \quad (10)$$

$$R_{st} = \frac{D_{sy} + D_s - 2D_{si}}{8\mu x_s L_{stk}}, \quad R_{sy} = \frac{\pi(D_{sy} + D_s)}{\mu L_{stk}(D_s - D_{sy})} \quad (11)$$

$$D_{ry} = \frac{2s_{rn}x_r}{\pi}$$
$$+ \sqrt{\left(\frac{2s_{rn}x_r}{\pi}\right)^2 + D_{ri}^2 - \frac{4s_{rn}}{\pi}(x_r D_{ri} + A_{fieldcoil})} \quad (12)$$

$$D_{sy} = \frac{2s_{sn}x_s}{\pi}$$
$$+ \sqrt{\left(\frac{2s_{sn}x_s}{\pi}\right)^2 + D_s^2 - \frac{4s_{sn}}{\pi}(x_s D_s - A_{armcoil})} \quad (13)$$

In the preceding equation, D_s and D_{si} are the outer and inner diameters of the stator, respectively. D_r and D_{ri} are the outer and inner diameters of the rotor, respectively, D_{sy} is the inner diameter of the stator yoke, D_{ry} is the outer diameter of the rotor yoke, L_{stk} is the stack length of the core, s_{sn} and s_{rn} are the number of stator slots and rotor slots, respectively, and x_s and x_r are the halved stator and rotor tooth widths, respectively. D_{si} can be determined by the rotor diameter D_r, and the air-gap lengths D_{sy} and D_{ry} are calculated using (12) and (13), respectively, accounting for the slot area determined from the current density and the number of turns in (3)–(6). The calculated magnetic resistance that varies with x_s, x_r, D_{sy}, and D_{ry} of the 8-pole/48-slot motor is shown in Fig. 3. Finally, x_s, x_r, D_{sy}, and D_{ry} should be determined from the minimum point of the total reluctances R_{sm} and R_{rm} of the motor.
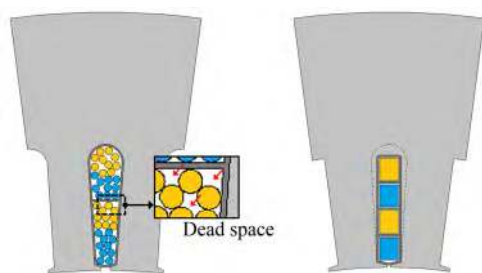

FIGURE 4. Conventional round wire and hairpin type rectangular wire.

IV. COPPER LOSS

A. ARMATURE COPPER LOSS
In this study, for a hairpin winding, the rectangular-wire type was used. This winding has several advantages. First, the gap between the tooth and coil is minimized reducing dead space. In other words, current density of the armature can be reduced by increasing the cross-sectional area of the wire. Consequently, as heat generated by the coil which is the copper loss is reduced, efficiency of motor can increase [17]. Second, a greater number of turns can be obtained in the same

FIGURE 5. Hairpin winding of the stator.

amount of space under the same conditions. In other words, less space is needed for the same number of turns as shown in Fig. 4. Therefore, the magnetic flux density of the stator can be decreased reducing iron loss. Consequently, in this study, the hairpin type rectangular wire is used for the purpose of improving the efficiency of the motor. Fig. 5 depicts the structure for the hairpin winding. Because the winding is assembled after the hairpin wire is formed, the manufacturing process is simplified and the end turn height can be uniform [17]. Meanwhile, in a high-speed machine, the high frequencies in AC current result in skin effect, as derived by (14). In order to avoid this effect, a sufficiently thin coil must be used.

$$\delta = \sqrt{\frac{1}{\pi f \mu_0 \mu_r \sigma}} \quad (14)$$

where δ and f are skin depth and frequency, respectively [21]. μ_0 and μ_r are the permeability of the free space and the relative magnetic permeability of the conductor, and σ denotes the conductivity of the conductor.

In other words, the skin depth is expressed in (14), and the winding thickness must be thinner than this depth. The frequency at the maximum speed of 10,000 rpm was 0.67 kHz, and the skin depth was approximately 2.44 mm. Thus, a rectangular wire of 2.9 mm × 3.5 mm was selected because the radius of the circumscribed circle of the rectangular wire is smaller than the calculated skin depth.

After the wire is selected, the copper loss can be calculated, even when accounting for the end coil. It is assumed that the coil is wound evenly inside the slot. Because distributed winding is applied to the stator, the average coil span A and temperature can be considered when calculating the resistance including that of the end coil as shown in Fig. 6(a). The stator's winding resistance can be expressed by the following equation:

$$R_a = \rho_c \cdot \frac{2 \cdot (L_{stk} + \pi(A/2)) \cdot N_{ph}}{\pi \cdot r_s^2} \cdot \left[1 + \alpha \cdot (T - 20°C)\right] \quad (15)$$

where N_{ph} is the number of turns in series per phase, respectively, r_s is the radius of the stator coil, T is the operating
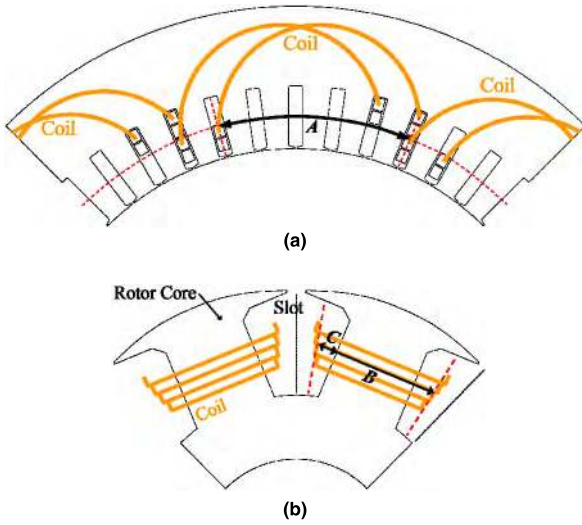
FIGURE 6. Average coil span *A* and *B*, and the average height *C* of the end coil (a) in stator and (b) in rotor.

temperature in °C, ρ_c is the resistivity of copper at 20°C, and α is the temperature coefficient of the resistivity. In the improved model, the end coil was shortened by the hairpin winding. And the improved model's phase resistance was 6.75 mΩ, which is 17% less than the prototype's resistance at 8.25 mΩ. This result suggests that copper loss can be reduced and increase the NEDC efficiency.

B. FIELD COPPER LOSS

The current induced to the field winding may fluctuate due to the armature reaction although the current of field winding is DC. The magnitude of these fluctuations might be small, but because the frequency is high, the skin effect is considered as well. The frequency of the current ripple at its maximum speed is approximately 4.6 kHz with an approximate skin depth of 0.97 mm. Therefore, a coil with a diameter of 0.95 mm, which is thinner than the skin depth, was used for the field winding. The field winding was wound around each tooth per pole. An analytical method was used to calculate the resistance in consideration of the end coil, as shown in Fig. 6(b). In the Fig. 6(b), the average coil span *B* and end-coil height *C* were assumed. The field winding resistance calculated with these values is derived as follows:

$$R_f = \rho_c \cdot \frac{2 \cdot (L_{stk} + B + 2C) \cdot N_f}{\pi \cdot r_r^2} \cdot \left[1 + \alpha \cdot (T - 20°C)\right]$$

(16)

where, N_f is the number of turns in the field winding, and r_r is the radius of the field coil of motor.

V. IRON LOSS
A. CORE MATERIAL SELECTION

A motor's performance at high speed is limited by iron loss. Iron loss is proportional to the magnetic flux density and frequency. It is important to minimize iron loss under load conditions. A silicon steel plate of 35PN230 with a thickness
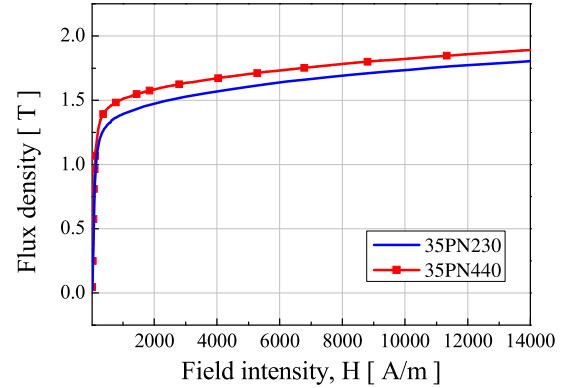

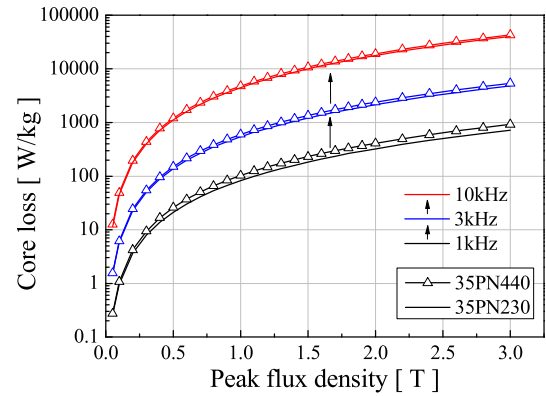**FIGURE 7.** B-H curves of the electrical steel 35PN230 and 35PN440.

FIGURE 8. Iron loss characteristics of the electrical steel 35PN230 and 35PN440.
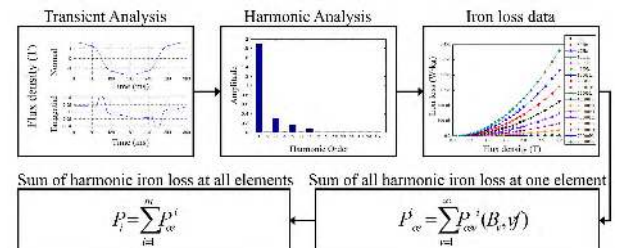

FIGURE 9. Calculation process of the iron loss.

of 0.35 mm was used for the prototype's stator and rotor. 30PN440 is an isotropic material and used in the improved model to minimize iron loss. As shown in Fig. 7, the electrical steel 35PN440 provides higher magnetic flux density about 8 % than 35PN230. Therefore, input current can be reduced to achieve the required torque. As a result, it is expected that the efficiency of the machine can be increased even though the core loss of the 35PN440 is slightly higher than that of the 35PN230 at the same condition as shown in Fig. 8.

B. IRON LOSS CALCULATION

Fig. 9 shows the method for calculating iron loss using the FEA. Five steps were used, in accordance with changes in the armature's input current and phase angle. The harmonics in the magnetic flux density in the radial and normal directions were taken into account up to the 30th order. This process
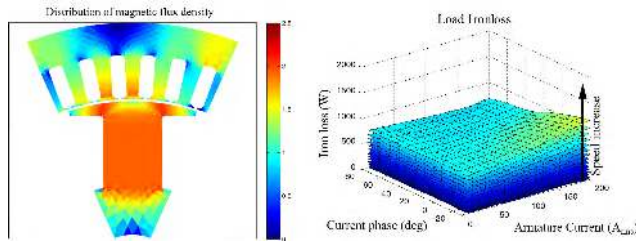
FIGURE 10. Iron loss distribution in the motor core, and iron loss according to the armature currents and currents phase angles.

was repeated for every renewal of field current. The process for calculating the iron loss is as follows [12], [22]:

1) Using nonlinear analysis of the finite elements, the magnetic flux density is calculated for each element for one period of the electrical angle. The magnetic flux density is calculated in the radial and tangential directions.

2) The previously calculated magnetic flux density is expanded into a Fourier series. The magnetic flux density is calculated with the amplitudes and phases divided for the fundamental and harmonic waves.

3) Using the iron-loss data from the electrical steel plate, the magnetic flux density and phase are calculated. Iron loss is calculated by taking account of the frequency, whose values are obtained from the experiment.

4) All of the iron loss in each element from fundamental and harmonic waves is calculated and summed. The iron loss in each element for one electrical angle period can be calculated.

5) The iron loss in all of the elements used in the FEA is added together. Thus, the iron loss for the motor under load can be calculated. The input current and phase of the field and armature are modified, and the process is repeated from Step 1.

Fig. 10 depicts the plot of iron loss with respect to the armature's input current and phase angle. Given the iron loss map, as the speed increases, iron loss does as well, and as the phase angle decreases, iron loss increases.

VI. DESIGN RESULT AND VERIFICATION

A. CHARACTERISTICS OF THE DESIGNED WFSM

In this study, the motor's performance was predicted based on an equivalent circuit. The performance can be predicted by using voltage and torque equations used to build the equivalent circuit [23], [24]. The voltage considering the iron loss obtained from the FEA was derived from (17) and (18):

$$\begin{bmatrix} v_d \\ v_q \end{bmatrix} = R_a \begin{bmatrix} i_{od} \\ i_{oq} \end{bmatrix} + \left(1 + \frac{R_a}{R_c}\right) \begin{bmatrix} v_{od} \\ v_{oq} \end{bmatrix}$$
$$+ p \begin{bmatrix} L_d & 0 \\ 0 & L_q \end{bmatrix} \begin{bmatrix} i_{od} \\ i_{oq} \end{bmatrix} \qquad (17)$$

$$\begin{bmatrix} v_{od} \\ v_{oq} \end{bmatrix} = \begin{bmatrix} 0 & -\omega L_q \\ \omega L_d & 0 \end{bmatrix} \begin{bmatrix} i_{od} \\ i_{oq} \end{bmatrix} + \begin{bmatrix} 0 \\ \sqrt{3}\omega\psi_f \end{bmatrix} \qquad (18)$$

The torque was calculated with (19) considering the mechanical loss determined experimentally

$$T = P_p\{(L_f I_f i_{oq}) + (L_d - L_q)i_{od}i_{oq}\} - (P_{mech}/\omega_m)$$
$$\times \begin{pmatrix} i_{od} = i_d - i_{cd}, & i_{oq} = i_q - i_{cq}, \\ i_{cd} = -\dfrac{\omega L_q i_{oq}}{R_c}, & i_{cq} = \dfrac{\omega(\psi_f + L_d i_{od})}{R_c} \end{pmatrix} \qquad (19)$$

where, i_d and i_q are the d- and q-axis armature currents, respectively, v_d and v_q are the d- and q-axis voltages, respectively, i_{od} and i_{oq} denote the currents subtracted the d- and q-axis currents resulting in the iron losses from the input currents i_d and i_q, respectively, R_a is the phase resistance of the armature winding, R_c is the equivalent resistance of the iron loss, L_d and L_q are the d- and q-axis inductances, respectively, p is the differential operator as d/dt, ψ_f is the *rms* flux linkage of the field winding, P_p is the number of pole-pairs, and ω and ω_m are the electrical and mechanical speeds, respectively, in rad/s. For the parameters in each equation, the field's magnetic flux, d, q-axis inductance, and iron loss under the load conditions were obtained via the nonlinear FEA; the operating point of the machine was calculated considering all load conditions.
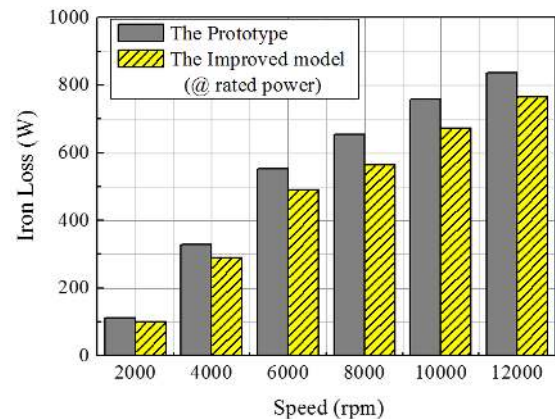

FIGURE 11. Iron loss of the prototype and improved model according to the speed.

Fig. 11 represents the iron loss calculated from the FEA. By using the iron loss and (20), iron loss resistance R_c can be calculated, and the calculated resistance was used in (17)-(19).

$$R_c = \frac{V_o^2}{P_{iron}} \text{(W)} \qquad (20)$$

The shaft, bearing, slip ring, and brush for the improved motor are the same as those of the prototype. Therefore, the mechanical loss obtained from the no-load test of the prototype, as described in Section II (*B*) can be used to design the improved motor as it is. Fig. 12 shows the measurements of mechanical loss tested at up to 9,000 rpm. Experimental mechanical loss values were interpolated as (21), and it was used to calculate torque by using (19). The loss is varied
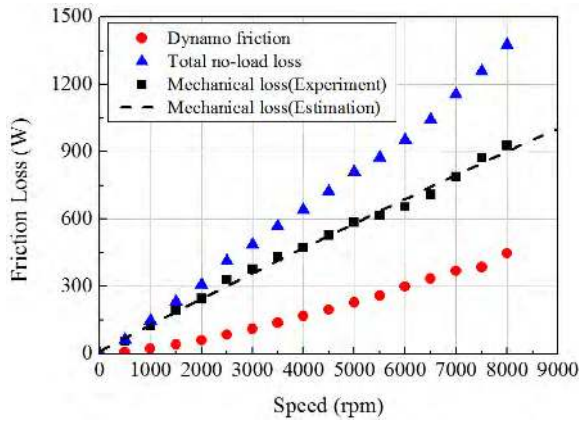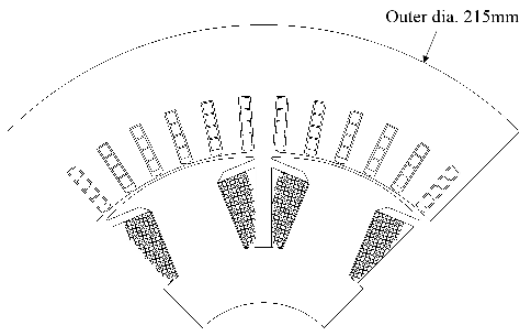
FIGURE 12. No-load test results.

FIGURE 13. The configuration of the improved motor as the proposed design result.

TABLE 2. Specifications of the designed motor.

Quantity	Unit	Value
Power	kW	120
Torque	Nm	280
Max. speed	rpm	10,000
Outer diameter	mm	215
Stack length	mm	118 (≤120)
Power density	kW/kg	2.32 (≥ 2.2)
Max. efficiency	%	96.5 (≥ 94)
Energy efficiency	%	94.4 (≥ 94)
Core material	-	35PN440

with speed, where n is the rotor speed in rpm. In this equation, n cannot be zero, or P_{mech} will also be zero.

$$P_{mech} = c_1 + c_2 \cdot n + c_3 \cdot n^2 (\text{W})$$
$$\times \begin{pmatrix} c_1 = 10.93643 \quad (\text{W}) \\ c_2 = 1.1876 \times 10^{-1} \quad (\text{W/rpm}) \\ c_3 = -9.33023 \times 10^{-7} \quad (\text{W/rpm}^2) \end{pmatrix} \quad (21)$$

The configuration of the improved motor as the proposed design result is shown in Fig. 13, and the specifications of the motor fulfilling the requirements are shown in Table 2. As the results, the stack length of the improved motor is 118 mm.
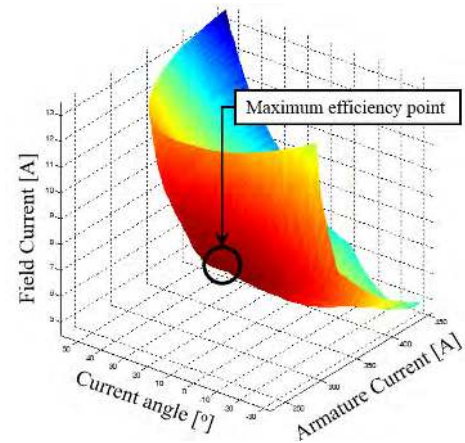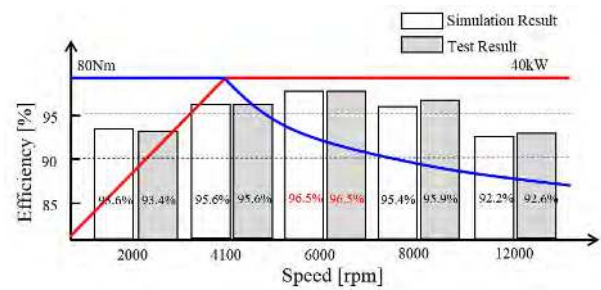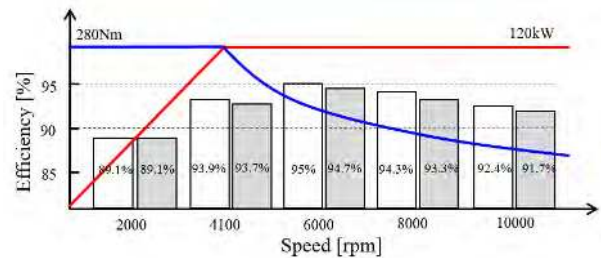

FIGURE 14. Output torque according to the armature current, current phase angle, and the field current.

FIGURE 15. Simulation and test results of the performance and the efficiency of the improved model (a) rated power and (b) maximum power.

It is the value decreased by 8.5 % comparing to 128 mm of the prototype.

To verify the validity of the design, the designed motor was set up and an experiment was conducted. The drive method of the motor was the maximum efficiency control as shown in Fig. 14. Fig. 15 provides a comparison between simulation results and test results of the torque and the efficiency at each speed. The reliability of the analytical results was verified with errors of less than 1% for the entire region. The motor's maximum efficiency at 40 kW and 6,000 rpm was 96.5%.

B. ENERGY EFFICIENCY
In this paper, the efficiency was calculated by considering the battery's input and output energy. Equation (22) provides the method for calculating energy efficiency where the efficiency
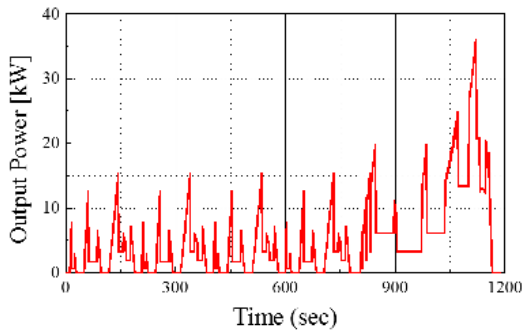
**FIGURE 16.** Output power variation in the NEDC mode.

TABLE 3. Energy efficiency in NEDC mode.

| Quantity	Unit	Prototype	Improved model	superior
Max. efficiency	%	96.5	96.5	-
Energy efficiency	%	93.7	94.4	**+ 0.7**

of the motor at its primary speeds can be predicted.

$$eff_{energy} = \frac{\int_0^t P_{out} dt}{\int_0^t P_{in} dt} \times 100(\%) \tag{22}$$

The NEDC was considered when calculating the energy efficiency in the main driving region. A vehicle's driving points in NEDC can be expressed in terms of the velocity and torque at that point, as shown in Fig. 1, Section I. As shown in Fig. 16, the unit of the velocity can be changed to rad/s, and that of the torque to Nm, generating a plot of the torque with respect to time. The results of the energy efficiency are shown in Table 3. The energy efficiency of the improved model was 0.7% higher that of the prototype despite the power density was increased. Fig. 17 shows the experimental values of the maps for the prototype and the improved WFSM comparing their respective efficiency. In Fig. 16(a) and (b), the maximum efficiency of the two models are the same. As shown in Fig. 17(c), however, in the region that includes the NEDC driving points, the improved model tended to be more efficient. The improved design was somewhat less efficient at high-velocity and -torque regions. Ultimately, enhancing the efficiency in the entire region was overly ambitious, but considering the pattern in the main driving region, the improved model demonstrated advantages in terms of the vehicle system. Fig. 18 presents the improved motor's volume, torque density, and efficiency. As a result of the proposed design, the volume of the designed model decreased and the power density and the efficiency in the NEDC cycle increased. The maximum output, torque, and velocity were equal to those of the prototype, and volume of the motor decreased by approximately 8.5% in order to increase the torque density. The motor's torque density thus increased by 8.5 %, from 2.12 kW/kg to 2.30 kW/kg.
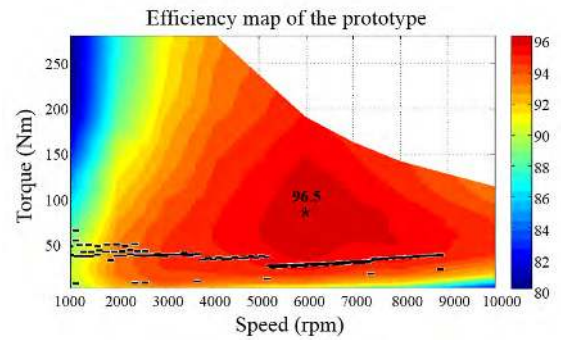
(a)
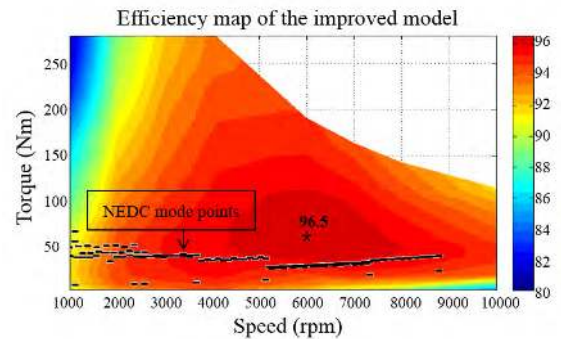
(b)
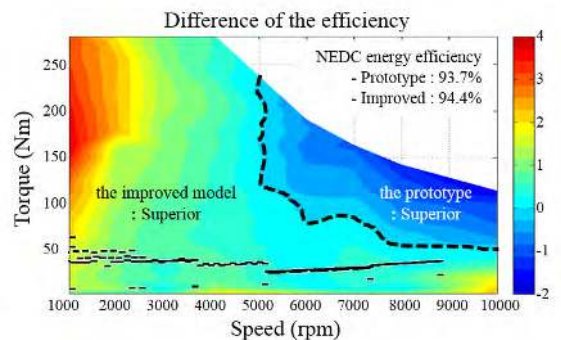
(c)

FIGURE 17. Efficiency map (a) of the prototype, (b) of the improved model, and (c) difference of the efficiency between the prototype and the improved model.
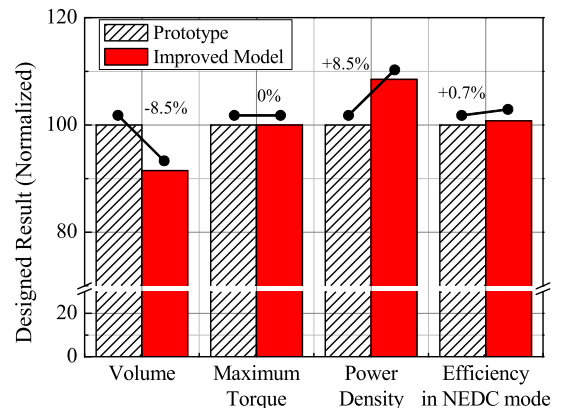

FIGURE 18. Comparison of the performance between the prototype and the improved model.

VII. CONCLUSION

This paper suggests a design method for 120 kW/10,000 rpm high-speed WFSM for vehicle traction. The appropriate core material was selected considering its material characteristics. In addition, the paper deals with design parameters such as the widths of the teeth and the yoke of the core and a hairpin-type armature winding, and it discussed methods for evaluating the mechanical, copper, and iron loss in order to maximize the efficiency in the NEDC based on FEA, experimental, and analytical approaches. The results indicate that the improved model was well designed and considered the pattern in the main driving region. Furthermore, a motor that fulfills the required specifications was designed. With the proposed method, the volume of this motor was reduced and the power density increased by approximately 8.5 %. In addition, energy efficiency increased by approximately 0.7 % considering the NEDC. Finally, the effectiveness of the motor was verified experimentally. Thus, it is expected that the performance of the electric vehicle system can be improved as a result of the proposed design method and using the designed motor.

REFERENCES

[1] K. I. Laskaris and A. G. Kladas, "Internal permanent magnet motor design for electric vehicle drive," *IEEE Trans. Ind. Electron.*, vol. 57, no. 1, pp. 138–145, Jan. 2010.

[2] M. Maier, J. Bacher, and A. Muetze, "Computation of induced voltages and currents in the field winding of wound-field synchronous machines under transient conditions," in *Proc. Int. Conf. Elect. Mach. (ICEM)*, Sep. 2014, pp. 86–92.

[3] A. K. Jain and V. T. Ranganathan, "Modeling and field oriented control of salient pole wound field synchronous machine in stator flux coordinates," *IEEE Trans. Ind. Electron.*, vol. 58, no. 3, pp. 960–970, Mar. 2011. doi: 10.1109/TIE.2010.2048295.

[4] P. Rasilo, A. Belahcen, and A. Arkkio, "Experimental determination and numerical evaluation of core losses in a 150-kVA wound-field synchronous machine," *IET Electric Power Appl.*, vol. 7, no. 2, pp. 97–105, Feb. 2013.

[5] J. Wang, X. Yuan, and K. Atallah, "Design optimization of a surface-mounted permanent-magnet motor with concentrated windings for electric vehicle applications," *IEEE Trans. Veh. Technol.*, vol. 62, no. 3, pp. 1053–1064, Mar. 2013.

[6] C. Liang, J. Wang, P. Lazari, and C. Xiao, "Optimizations of a permanent magnet machine targeting different driving cycles for electric vehicles," in *Proc. IEEE Int. Electr. Mach. Drives Conf. (IEMDC)*, May 2013, pp. 855–862.

[7] K. Kiyota, H. Sugimoto, and A. Chiba, "Comparison of energy consumption of SRM and IPMSM in automotive driving schedules," in *Proc. IEEE ECCE*, Sep. 2012, pp. 853–860.

[8] L. Chen, J. Wang, P. Lombard, P. Lazari, and V. Leconte, "Design optimisation of permanent magnet assisted synchronous reluctance machines for electric vehicle applications," in *Proc. Int. Conf. Electr. Mach. (ICEM)*, Sep. 2012, pp. 2647–2653.

[9] R. Mbayed, G. Salloum, L. Vido, E. Monmasson, and M. Gabsi, "Optimal control of the hybrid excitation synchronous machine for electric propulsion in electric vehicle," in *Proc. 15th Eur. Conf. Power Electron. Appl. (EPE)*, Sep. 2013, pp. 1–10.

[10] S. Gunther, S. Ulbrich, and W. Hofmann, "Driving cycle-based design optimization of interior permanent magnet synchronous motor drives for electric vehicle application," in *Proc. Int. Symp. Power Electron., Electr. Drives, Autom. Motion (SPEEDAM)*, Jun. 2014, pp. 25–30.

[11] G. Pellegrino, P. Guglielmi, A. Vagati, and F. Villata, "Core losses and torque ripple in IPM machines: Dedicated modeling and design tradeoff," *IEEE Trans. Ind. Appl.*, vol. 46, no. 6, pp. 2381–2391, Nov. 2010.

[12] B. H. Lee, S. O. Kwon, T. Sun, J. P. Hong, G. H. Lee, and J. Hur, "Modeling of core loss resistance for d-q equivalent circuit analysis of IPMSM considering harmonic linkage flux," *IEEE Trans. Magn.*, vol. 47, no. 5, pp. 1066–1069, May 2011.

[13] P. Rasilo, A. Belahcen, and A. Arkkio, "Importance of iron-loss modeling in simulation of wound-field synchronous machines," *IEEE Trans. Magn.*, vol. 48, no. 9, pp. 2495–2504, Sep. 2012.

[14] Z. Shi *et al.*, "Torque analysis and dynamic performance improvement of a PMSM for EVs by skew angle optimization," *IEEE Trans. Appl. Supercond.*, vol. 29, no. 2, Mar. 2019, Art. no. 0600305.

[15] X. Sun *et al.*, "Performance improvement of torque and suspension force for a novel five-phase BFSPM machine for flywheel energy storage systems," *IEEE Trans. Appl. Supercond.*, vol. 29, no. 2, Mar. 2019, Art. no. 0601505.

[16] X. Sun *et al.*, "Performance analysis of suspension force and torque in an IBPMSM with V-shape PMs for flywheel batteries," *IEEE Trans. Magn.*, vol. 54, no. 11, Nov. 2018, Art. no. 8105504.

[17] D. S. Jung, Y. H. Kim, U. H. Lee, and H. D. Lee, "Optimum design of the electric vehicle traction motor using the hairpin winding," in *Proc. IEEE 75th Veh. Technol. Conf. (VTC Spring)*, May 2012, pp. 1–4.

[18] X. Sun, Y. Shen, S. Wang, G. Lei, Z. Yang, and S. Han, "Core losses analysis of a novel 16/10 segmented rotor switched reluctance BSG motor for HEVs using nonlinear lumped parameter equivalent circuit model," *IEEE/ASME Trans. Mechatronics*, vol. 23, no. 2, pp. 747–757, Apr. 2018.

[19] D. C. Hanselman and W. H. Peake, "Eddy-current effects in slot-bound conductors," *IEE Proc. Electric Power Appl.*, vol. 142, no. 2, pp. 131–136, Mar. 1995.

[20] P.-D. Pfister and Y. Perriard, "Very-high-speed slotless permanent-magnet motors: Analytical modeling, optimization, design, and torque measurement methods," *IEEE Trans. Ind. Electron.*, vol. 57, no. 1, pp. 296–303, Jan. 2010.

[21] H. M. Hamalainen, J. J. Pyrhonen, and J. Puranen, "Minimizing skin effect in random wound high speed machine stator," *IEEE EUROCON*, vol. 09, pp. 752–757, May 2009.

[22] G. H. Kang, J. P. Hong, G. T. Kim, and J. W. Park, "Improved parameter modeling of interior permanent magnet synchronous motor based on finite element analysis," *IEEE Trans. Magn.*, vol. 36, no. 4, pp. 1867–1870, Jul. 2000.

[23] M.-S. Lim, S.-H. Chai, and J.-P. Hong, "Design and iron loss analysis of sensorless-controlled interior permanent magnet synchronous motors with concentrated winding," *IET Electr. Power Appl.*, vol. 8, no. 9, pp. 349–356, Nov. 2014.

[24] M. S. Lim, S. H. Chai, J. S. Yang, and J. P. Hong, "Design and verification of 150 krpm PMSM based on experiment results of prototype," *IEEE Trans. Ind. Electron.*, vol. 62, no. 12, pp. 7827–7836, Dec. 2015.

HYEON-JIN PARK received the Bachelor's degree in Mechanical Engineering from Hanyang University, Seoul, South Korea, in 2011. From 2014 to 2017, he was a Research Engineer in Keyang, South Korea. Currently, he is an integrated Master's degree and Ph.D. student in Automotive Engineering from Hanyang University, Seoul, South Korea. His research interests are electromagnetic field analysis and electric machine design.

MYUNG-SEOP LIM received the Bachelor's degree in Mechanical Engineering from Hanyang University, Seoul, South Korea, in 2012. Also, he received the Master's and Ph.D. degree in Automotive Engineering from the Same University, in 2014 and 2017, respectively.

From 2017 to 2018, he was a Research Engineer in Hyundai Mobis, Yongin, South Korea. Since 2018, he has been with Yeungnam University, Gyeongbuk, South Korea, where he is currently an Assistant Professor. His research interests include electromagnetic field analysis and electric machinery for mechatronics systems such as automotive and robot applications.

• • •